Dalton Transactions

PAPER

Cite this: *Dalton Trans.*, 2017, **46**, 7878

Temperature dependent NIR emitting lanthanide-PMO/silica hybrid materials†

Anna M. Kaczmarek, *‡[a] Dolores Esquivel, ‡[b] Judith Ouwehand,[c] Pascal Van Der Voort, [c] Francisco J. Romero-Salguero [b] and Rik Van Deun *[a]

Received 3rd May 2017,
Accepted 5th June 2017

DOI: 10.1039/c7dt01620d

rsc.li/dalton

Two materials – a mesoporous silica (MS) and a periodic mesoporous organosilica (PMO) functionalized with dipyridyl-pyridazine (dppz) units were grafted with near-infrared (NIR) emitting lanthanide (Nd^{3+}, Er^{3+}, Yb^{3+}) complexes in an attempt to obtain hybrid NIR emitting materials. The parent materials: dppz-vSilica and dppz-ePMO were prepared by a hetero Diels–Alder reaction between 3,6-di(2-pyridyl)-1,2,4,5-tetrazine (dptz) and the double bonds of either ethenylene-bridged PMO (ePMO) or vinyl-silica (vSilica) and subsequent oxidation. The dppz-vSilica is reported here for the first time. The prepared lanthanide-PMO/silica hybrid materials were studied in depth for their luminescence properties at room temperature and chosen Nd^{3+} and Yb^{3+} samples also at low temperature (as low as 10 K). We show that both the dppz-vSilica and dppz-ePMO materials can be used as "platforms" for obtaining porous materials showing NIR luminescence. To obtain NIR emission these materials can be excited either in the UV or Vis region (into the $\pi \rightarrow \pi^*$ transitions of the ligands or directly into the f–f transitions of the Ln^{3+} ions). More interestingly, when functionalized with Nd^{3+} or Yb^{3+} β-diketonate complexes these materials showed interesting luminescence properties over a wide temperature range (10–360 K). The Yb^{3+} materials were investigated for their potential use as ratiometric temperature sensors.

1. Introduction

The remarkable luminescence properties of lanthanide ions (Ln^{3+}) are largely due to the well-shielded nature of the f–f transitions.[1–3] Ln^{3+} ions show characteristic narrow line like emission peaks ranging from the ultraviolet-visible (UV-Vis) to near-infrared (NIR) region, as well as exhibit relatively long luminescence lifetimes. Yet, because the f–f transitions of lanthanides are parity forbidden, their absorption coefficients are very low and as a result of this they exhibit low emission intensities. In order to overcome this problem various inorganic materials and hybrid organic–inorganic materials, which allow exciting the Ln^{3+} ions through charge-transfer bands or organic ligands, have been designed.[4] This has led scientists to explore various Ln^{3+} hybrid systems, which could lead to very efficient luminescent materials additionally showing high processability. Among them organic functionalized mesoporous silica (MS) and periodic mesoporous organosilica (PMO) materials have attracted particular attention as hybrid hosts for lanthanide complexes and very recently lanthanide polyoxometalates (POMs) for the very first time.[5–10] Well-ordered nanoporous structures, large surface areas and possibility of incorporating functional organic groups make both organic–inorganic hybrid materials promising supports for binding Ln^{3+} compounds.

Mesoporous silicas (MS) such as MCM-41 and SBA-15 have been functionalized with chelating organic ligands, including modified β-diketonates, pyridyl groups, 1,10-phenathroline and calix[4]arene derivatives.[11–17] Other suitable sensitizer ligands as bipyridine, acridone, mercaptobenzoic acid or 2-phenoyltrifluoroacetonate have been successfully incorporated as bridging organic compounds into PMO framework.[18–21] Recently, we have reported the incorporation of dipyridyl-dihydropyridazine moieties on the surface through hetero Diels–Alder reaction between the double bonds on an ethenylene-bridged PMO and a tetrazine derivative.[5] Tetrazine-derived ligands can be employed as sensitizers for Ln^{3+} ions and due to their low triplet level they can be well matched with the accepting levels of NIR emitting lanthanides such as Nd^{3+}, Er^{3+}, Yb^{3+}. For example the 3,6-bis(2-pyridyl)tetrazine ligand together with thenoyltrifluoroacetone have been used

[a]*L*[3] *Luminescent Lanthanide Lab, Department of Inorganic and Physical Chemistry, Ghent University, Krijsglaan 281-S3, B-9000 Ghent, Belgium. E-mail: anna.kaczmarek@ugent.be, rik.vandeun@ugent.be*
[b]*Departamento de Química Orgánica, Instituto Universitario de Investigación en Química Fina y Nanoquímica IUIQFN, Facultad de Ciencias, Universidad de Córdoba, Campus de Rabanales, Edificio Marie Curie, E-14071 Córdoba, Spain*
[c]*COMOC, Department of Inorganic and Physical Chemistry, Ghent University, Krijsglaan 281-S3, B-9000 Ghent, Belgium*

†Electronic supplementary information (ESI) available: N_2 sorption isotherms, additional luminescence data. See DOI: 10.1039/c7dt01620d

‡These authors contributed equally to the work.

for obtaining NIR emitting complexes with Nd^{3+}, Er^{3+}, and Yb^{3+}.[22]

A precise measurement of temperature can be crucial in various fields of application, such as cryogenics, safety sector, biology, medicine, engineering or chemical reaction monitoring, to give a few examples.[23–25] The traditional, so-called contact thermometers, are not suitable for temperature measurements of fast-moving objects or at the submicron scale (such as in microfluids, microcircuits or in cells). Due to the constraints of conventional thermometers many new thermometers based on various optical methods are being developed.[26] Among them much attention is being given to luminescence based thermometry and various materials such as quantum dots, lanthanide doped inorganic phosphors, lanthanide doped semiconductors, lanthanide MOFs or fluorescent polymers have shown promising results, to give a few examples.[27–29] There are various ways of assessing the temperature or temperature change of a material by employing luminescence features. Most often the steady state intensity of one (or two) transition(s), or the luminescence lifetime is used.[30] As Ln^{3+} emission in the NIR region is in general much weaker then in the Vis region, NIR emitting thermometers are substantially less frequently reported.

In this work we report the preparation of a mesoporous silica and a periodic mesoporous organosilica material, which are both functionalized with dipyridyl-pyridazine (dppz) units by a hetero Diels–Alder reaction between the substituted tetrazine (3,6-di(2-pyridyl)-1,2,4,5-tetrazine) and the double bonds of either vinyl-silica or ethenylene-bridged PMO. We have previously reported a similar material – a dpdp-ePMO@Eu (dpdp = dipyridyl-dihydropyridazine) and studied its luminescence properties in the Vis region.[5] Here we prepare a modified dppz-ePMO and novel dppz-vSilica material. These two materials are further grafted with Nd^{3+}, Er^{3+}, and Yb^{3+} β-diketonate complexes in an attempt to obtain hybrid NIR emitting materials. Additionally, we study the temperature dependent luminescence properties of dppz-ePMO and dppz-vSilica materials functionalized with β-diketonate complexes of Nd^{3+} and Yb^{3+}.

2. Experimental section

All reactants and solvents were used as received without further purification.

2.1. Synthesis

Synthesis of 3,6-di(2-pyridyl)-1,2,4,5-tetrazine. The tetrazine derivative was synthesized according to the following procedure, which is a modified synthesis based on that previously reported in literature.[31] 10.0 g (96.0 mmol) 2-cyanopyridine and 15.1 g (300 mmol) hydrazine hydrate were stirred for 16 h at 90 °C in an inert atmosphere. The mixture was then cooled to room temperature and filtered and washed with water and then ethanol and dried under vacuum. Orange dihydrotetrazine was obtained. 200 mg (0.828 mmol) of dihydrotetrazine was suspended in 6 mL of acetic acid and stirred on a magnetic stirrer. 174 mg (2.52 mmol) of sodium nitrite was added in small portions to the solution and an immediate color change from orange to dark red was observed. After the reaction was completed the solution was slowly poured into a beaker filled with ice. At this point the color changed from red to dark purple-red. The product was left to crystallize for several minutes. It was next isolated by filtration and the residue was washed with water (20 mL) and dried *in vacuo* to yield 3,6-bis(2-pyridyl)tetrazine as a purple solid.

The compound was characterized by elemental analysis (calculated: 61.07% C, 3.41% H, 35.58% N; found: 60.43% C, 3.22% H, 35.88% N).

Synthesis of dipyridyl-pyridazine functionalized ethenylene-bridged PMO (dppz-ePMO), see Scheme 1. The surface Diels–Alder reaction of an ethenylene-bridged PMO (ePMO) with 3,6-di(2-pyridyl)-1,2,4,5-tetrazine as diene was carried out following a method already reported by Esquivel *et al.* for the formation of surface Diels–Alder adducts on periodic mesoporous organosilicas.[5] In a typical procedure 0.3 g of 100% *trans* ethenylene-bridged PMO (ePMO),[32] previously heated under vacuum at 120 °C overnight, was added to a mixture of 0.25 g tetrazine derivative dissolved in 20 ml of dodecane. The mixture was aged in an autoclave at 200 °C for 11 days. After cooling down the solid was filtered and washed several times with chloroform. Additionally, in order to remove possible diene physically adsorbed into the pores, the material was refluxed in chloroform for 8 h (this procedure was repeated two times). The solid product was collected on a filter, washed with chloroform and acetone and dried at 120 °C under vacuum. Last, the product was aromatized using $NaNO_2$ following procedures previously reported.[33] The procedure was repeated two times, and the material was washed excessively and dried at 120 °C under vacuum afterwards. The nitrogen content on dppz-ePMO material was 1.0% (based on CHN results).

Synthesis of dipyridyl-pyridazine functionalized vinyl silica (dppz-vSilica), see Scheme 1. The vSilica material was synthesized according to the following procedure. 7.00 g of P123 was dissolved in 210 mL 2 M HCl and left to stir for 45 minutes at room temperature (until completely dissolved). Next, 13.1 mL of TEOS was added and the solution was stirred 45 minutes at 40 °C. Then 3.1 mL of vinyltriethoxysilane (VTES) was added and stirred for 20 h. A white precipitate was formed and left to age at 100 °C for 24 h. After filtering and washing with water and ethanol the surfactant was extracted three times from a mixture of ethanol and 1 M HCl in appropriate amounts. The product was dried under vacuum at 120 °C overnight. The dppz-vSilica material was obtained in a similar approach as that described for the preparation of dppz-ePMO, yet in milder conditions. To obtain the desired product a flask reaction (under nitrogen) was carried out (set at 120 °C for 7 days). The nitrogen content on dppz-vSilica material was 0.65% (based on CHN results).

Synthesis of dppz-ePMO material grafted with $LnCl_3$ (dppz-ePMO@$LnCl_3$). For the preparation of the dppz-ePMO@$LnCl_3$

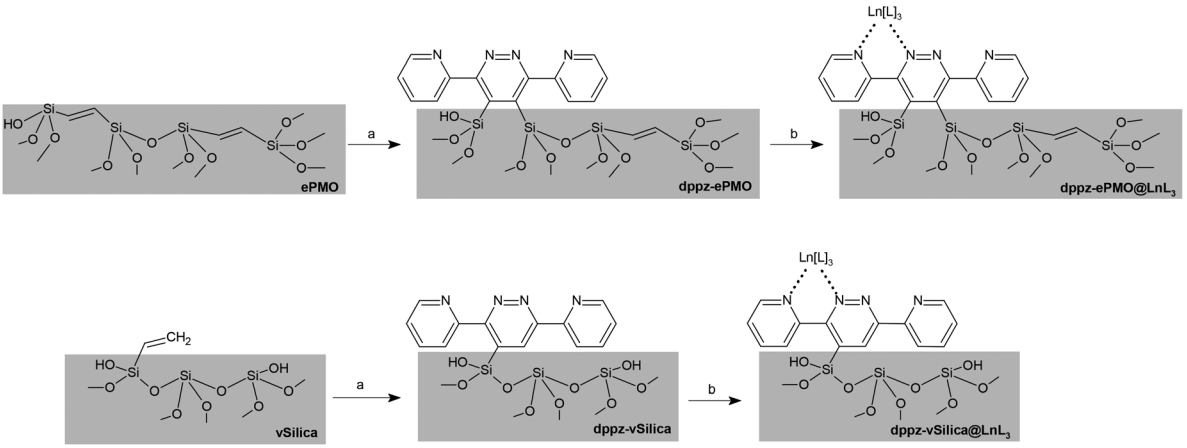

Scheme 1 Synthesis of dppz-ePMO/vSilica@LnL_3 materials.

materials, a certain amount of $LnCl_3{\cdot}6H_2O$ (Ln = Nd^{3+}, Er^{3+}, Yb^{3+}) was dissolved in 20 mL methanol and then dppz-ePMO was added to this solution. The molar ratio of $LnCl_3$ to dppz-ePMO was 4 : 1. The mixture was stirred for 10 minutes at room temperature. Next it was sealed in glass tubes and placed on a heating block set at 120 °C for 24 h. After cooling to room temperature the product was filtered and washed several times with methanol (in order to remove any physisorbed lanthanide salt). The product was dried in a vacuum oven at 50 °C.

Synthesis of dppz-vSilica material grafted with $LnCl_3$ (dppz-vSilica@$LnCl_3$). For the preparation of the dppz-vSilica@$LnCl_3$ materials, a certain amount of $LnCl_3{\cdot}6H_2O$ (Ln = Nd^{3+}, Er^{3+}, Yb^{3+}) was dissolved in 20 mL methanol and then dppz-vSilica was added to this solution. The molar ratio of $LnCl_3$ to dppz-ePMO was 4 : 1. The mixture was left to stir for 3 h on a magnetic stirrer with heating at 50 °C. The dppz-vSilica@$LnCl_3$ materials were prepared at lower temperatures and the reactions were carried out for a shorter time compared to the dppz-ePMO@$LnCl_3$ materials, due to the lower thermal stability of MS materials. After cooling to room temperature the product was filtered and washed several times with methanol. The product was dried in a vacuum oven at 50 °C.

Synthesis of $Ln(tta)_3{\cdot}2H_2O$ and $Ln(bta)_3{\cdot}2H_2O$ complexes (Ln = Nd^{3+}, Er^{3+}, Yb^{3+}). The complexes were prepared according to previously reported procedures.[34,35] The complexes were characterized by elemental analysis.

$Nd(tta)_3{\cdot}2H_2O$ ($NdC_{24}H_{16}F_9O_8S_3$) calculated: 34.16% C; 1.91% H; found: 35.03% C; 2.15% H. $Er(tta)_3{\cdot}2H_2O$ ($ErC_{24}H_{16}F_9O_8S_3$) calculated: 33.25% C; 1.86% H; found: 34.10%% C; 1.92% H.

$Yb(tta)_3{\cdot}2H_2O$ ($YbC_{24}H_{16}F_9O_8S_3$) calculated: 33.03% C; 1.85% H; found: 33.87% C; 2.08% H. $Nd(bta)_3{\cdot}2H_2O$ ($NdC_{30}H_{22}O_8F_9$) calculated: 43.64% C; 2.69% H; found: 43.89% C; 2.85% H.

$Er(bta)_3{\cdot}2H_2O$ ($ErC_{30}H_{22}O_8F_9$) calculated: 42.45% C; 2.61% H; found: 43.06% C; 2.80% H. $Yb(bta)_3{\cdot}2H_2O$ ($YbC_{30}H_{22}O_8F_9$) calculated: 42.17% C; 2.59% H; found: 42.51% C; 2.88% H.

Synthesis of dppz-ePMO material grafted with $Ln(tta)_3$/$Ln(bta)_3$ complexes (dppz-ePMO@$Ln(tta)_3$ and dppz-ePMO@$Ln(bta)_3$), see Scheme 1. A similar procedure was used as for the synthesis of dppz-ePMO@$LnCl_3$ except that $Ln(tta)_3$or $Ln(bta)_3$ complexes were used. The molar ratio of Ln^{3+} complexes to dppz-ePMO was maintained at 4 : 1.

Synthesis of dppz-vSilica material grafted with $Ln(tta)_3$/$Ln(bta)_3$ complexes (dppz-vSilica@$Ln(tta)_3$ and dppz-vSilica@$Ln(bta)_3$), see Scheme 1. A similar procedure was used as for the synthesis of dppz-vSilica@$LnCl_3$ except that $Ln(tta)_3$or $Ln(bta)_3$ complexes were used. The molar ratio of Ln^{3+} complexes to dppz-vSilica was maintained at 4 : 1.

2.2. Characterization

XRD patterns were recorded by a Bruker D8 DISCOVER A25 diffractometer or Thermo Scientific ARL X'TRA diffractometer equipped with a Cu Kα (λ = 1.5405 Å) source, a goniometer and a Peltier cooled Si (Li) solid state detector.

Nitrogen adsorption–desorption isotherms were measured by using a Micromeritics TriStar 3000 analyzer at −196 °C. The samples were vacuum dried for 24 h at 120 °C before the measurements. Surface areas were calculated using the Brunauer–Emmett–Teller (BET) method. Pore size distributions were obtained by analysis of the desorption branch of the isotherms using the Barrett–Joyner–Halenda (BJH) method.

The ^{13}C MAS NMR spectra were recorded at 100.61 MHz on a Bruker AVANCE-400 WB dual channel NMR spectrometer at room temperature. An overall of 1000 free induction decays were accumulated. The excitation pulse and recycle time were 6 ms and 2 s. Chemical shifts were measured relative to tetramethylsilane standard. All samples were dried at 120 °C for 24 h prior to analysis.

Elemental analysis (CHNS) was performed on a Thermo Flash 2000 elemental analyzer by using V_2O_5 as catalyst.

The luminescence of solid samples was studied. Solid powdered samples were put between quartz plates (Starna cuvettes for powdered samples, type 20/C/Q/0.2).

Luminescence measurements were performed on an Edinburgh Instruments FLSP920 UV-vis-NIR spectrometer setup using a 450 W xenon lamp as the steady state excitation source and a Hamamatsu R5509-72 photomultiplier operating at −80 °C. The time-resolved measurements were performed using a Continuum Surelite I laser (450 mJ @1064 nm), operating at a repetition rate of 10 Hz and using the third harmonic (355 nm) as the excitation source, and the photomultiplier detector mentioned above. The temperature dependent measurements were measured using an ARS closed cycle cryostat at a temperature range between 10 K–360 K (with a temperature step of 60 K).

The luminescence decay curves of the samples were measured when excited into the maximum of the ligand band and monitored at the appropriate wavelength. The decay curves could be well fitted using a double-exponential function.

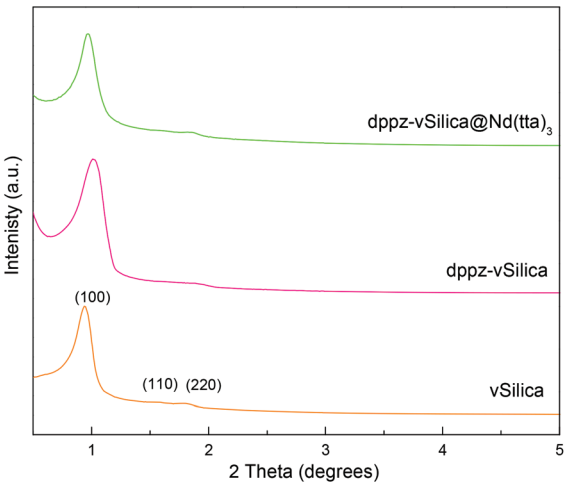

Fig. 2 Powder XRD patterns of vSilica, dppz-vSilica, and dppz-vSilica@Nd(tta)$_3$.

3. Results and discussion

The Ln^{3+}-dppz-ePMO/vSilica hybrid materials (Ln = Nd^{3+}, Er^{3+}, Yb^{3+}) were obtained in two steps (Scheme 1). First, the successful formation of dppz-ePMO/vSilica through Diels–Alder cycloaddition between the double bonds of the ePMO/vSilica and 3,6-di(2-pyridyl)tetrazine was carried out (step a in Scheme 1). Next, these materials (dppz-ePMO/vSilica) were further functionalized with Ln^{3+} β-diketonate complexes giving rise to NIR emitting hybrid porous materials (step b in Scheme 1).

3.1. Dipyridyl-pyridazine functionalized parent materials (dppz-ePMO and dppz-vSilica)

To characterize the materials, powder X-ray diffraction analysis was performed on ePMO, dppz-ePMO, vSilica and dppz-vSilica as shown in Fig. 1 and 2. For both the dppz-ePMO and dppz-vSilica a strong reflection (100) at low 2θ as well as two small second-order reflection peaks (110) and (200) are observed. This is typical for materials with a hexagonal arrangement of uniform pores. The X-ray diffraction patterns of the dppz-ePMO and dppz-vSilica are almost unchanged when compared to the parent materials (ePMO and vSilica, respectively). This indicates that the ordered hexagonal mesostructure (*P6mm*) is retained after the hetero Diels–Alder reactions.

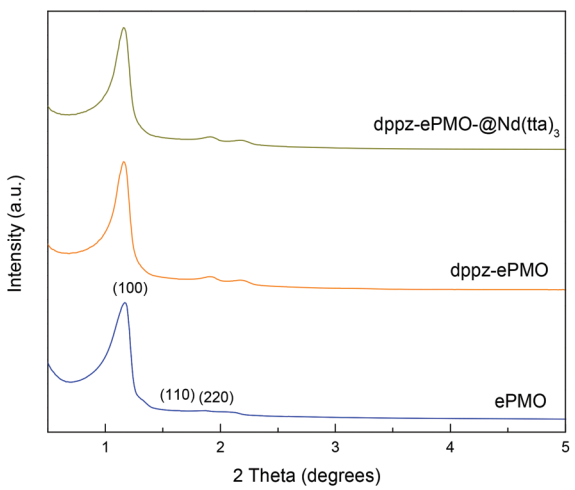

Fig. 1 Powder XRD patterns of ePMO, dppz-ePMO, and dppz-ePMO@Nd(tta)$_3$.

The N_2 adsorption–desorption isotherms of ePMO, dppz-ePMO, vSilica and dppz-vSilica are shown in Fig. S1.† Both parent materials (ePMO and vSilica) exhibit type IV isotherms with H1-type hysteresis loops at relative pressures in the range 0.5–0.8, characteristic of mesoporous materials with uniform mesopores. The BET surface areas, pore volumes and pore diameters are 722 $m^2\ g^{-1}$, 0.78 $cm^3\ g^{-1}$ and 5.8 nm, for ePMO and 805 $m^2\ g^{-1}$, 0.92 $cm^3\ g^{-1}$ and 5.4 nm for vSilica, respectively. After functionalization, dppz-ePMO and dppz-vSilica showed similar nitrogen adsorption–desorption isotherms, which confirmed their mesoporous structure. A pronounced decrease of the surface area, pore volume and pore size was observed after the formation of surface Diels–Alder adducts. These results confirm the phenomenon of surface decoration into the pores of ePMO and vSilica with Diels–Alder adducts, previously reported in this type of reaction with other dienes.[36]

The solid-state ^{13}C CP/MAS NMR spectrum of the vSilica material showed two intense signals at 138 and 130 ppm corresponding to the sp^2 carbons of the vinyl groups grafted on the silica surface (Fig. 3). Additional signals of residual surfactant (76 and 71 ppm) and non-hydrolyzed ethoxy groups (58 and 18 ppm) were present. After the Diels–Alder reaction with the tetrazine derivative, dppz-vSilica showed new bands in the aromatic region (160–120 ppm) confirming the successful formation of the surface Diels–Alder adduct. Additionally, signals at 6 and 19 ppm were assigned to Si–CH_2–CH_3 functionalities formed under the reaction conditions.[37] The ^{13}C CP/MAS NMR spectrum of the dppz-ePMO material corroborated the results obtained in our previous work.[5]

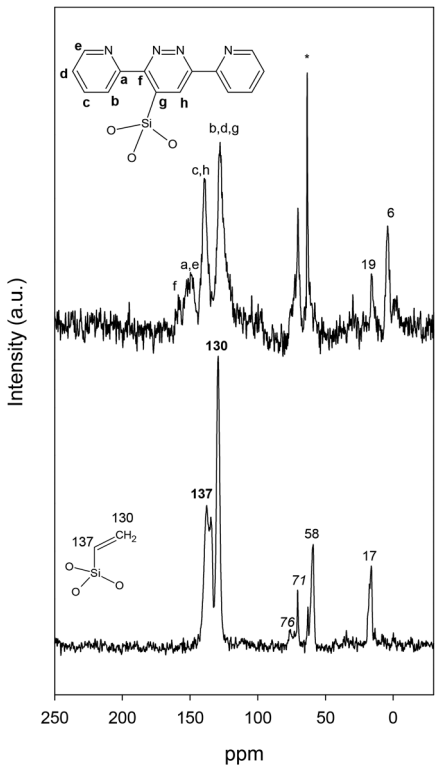

Fig. 3 ^{13}C CP/MAS NMR of vSilica and dppz-vSilica (*, ethanol residues).

3.2. Structural characterization of Ln^{3+}-dppz-ePMO/vSilica hybrid materials (Ln = Nd^{3+}, Er^{3+}, Yb^{3+})

After binding of Ln^{3+} to dppz-ePMO and dppz-vSilica, all resulting materials remained intact the ordered hexagonal mesostructure. The powder XRD patterns of dppz-ePMO and dppz-vSilica bonded to $Nd(tta)_3$ are shown in Fig. 1 and 2, respectively. Likewise, the surface properties are maintained after grafting with lanthanide complexes.[5]

3.3. Luminescence properties of Ln^{3+} functionalized dppz-ePMO/vSilica hybrid materials (Ln = Nd^{3+}, Er^{3+}, Yb^{3+})

In our previous work we have studied the luminescence properties of ePMO functionalized with dipyridyl-dihydropyridazine and further with Eu^{3+} ions (in the form of $EuCl_3$ or $Eu(tta)_3$ complex). We observed that both in the case of the $EuCl_3$ and $Eu(tta)_3$ functionalized materials energy is not completely transferred from the dipyridyl-dihydropyridazine (dpdp) ligand to the Eu^{3+} ions. This suggests that the triplet level of the ligand is located only slightly higher than the accepting level of Eu^{3+} (18 674 cm^{-1}) and that it could be a ligand very well suited for the design of NIR emitting Nd^{3+}, Er^{3+} and Yb^{3+} materials.

The dpdp (previously employed for the preparation of our Eu@PMO materials) and dppz ligands are very similar and we do not expect many differences in their energy harvesting ability or triplet level.[5] Here, we have prepared dppz-ePMO and dppz-vSilica materials (the dppz-vSilica material is new, synthesized for the first time in this work) functionalized with β-diketonate complexes of Nd^{3+}, Er^{3+} and Yb^{3+} and investigated their NIR luminescence properties in detail. Two β-diketonate ligands were chosen for the study – 2-thenoyltrifluoroacetone (tta; triplet level: 20 400 cm^{-1}) and benzoyltrifluoroacetone (bta; 21 600 cm^{-1}). These β-diketonate ligands have a double function in these materials. First of all, they shield the first coordination sphere of the Ln^{3+} ion from H_2O molecules and quenching groups and second they provide an additional ligand through which they can be excited. Ligands with C–F groups instead of C–H groups have been chosen to prevent the quenching of the NIR emission. The combined excitation–emission spectra of all these complexes have been presented in the ESI (Fig. S2–S4†). The importance of NIR Ln^{3+} and their use for silica-based materials has previously been extensively visualized by numerous publications.[38–42] These kind of materials can find applications in bio-imaging, bio-sensing, in laser systems, fiber-optic communications, thermometers, *etc*.

Fig. 4 presents the combined excitation–emission spectra of the Nd^{3+} β-diketonate functionalized dppz-ePMO and dppz-vSilica compounds. For the sake of comparison the dppz-ePMO and dppz-vSilica materials were also functionalized with the $NdCl_3$ salt and the luminescence spectra of these materials have been presented in the ESI (Fig. S5 and S6†). It can clearly be seen that the dppz-ePMO@NdL_3 materials differ from the dppz-ePMO@$NdCl_3$ and dppz-vSilica@$NdCl_3$ materials. In the excitation spectra of the dppz-ePMO@NdL_3 and dppz-vSilica@NdL_3 materials a broad band in the range 250–500 nm is present, attributed to the $\pi \rightarrow \pi^*$ transitions of the ligands. The maximum of this broad band varies a bit for each of the samples and seems to be partially dependent of the employed β-diketonate ligand. In the materials where

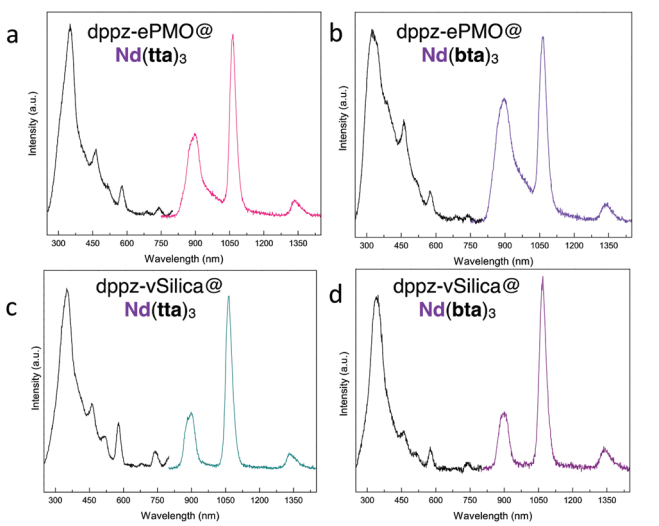

Fig. 4 Combined excitation–emission luminescence spectra of (a) dppz-ePMO@Nd(tta)$_3$, (b) dppz-ePMO@Nd(bta)$_3$, (c) dppz-vSilica@Nd(tta)$_3$, and (d) dppz-vSilica@Nd(bta)$_3$. All of the emission spectra where recorded when excited into the maximum of the broad bands and observed at the $^4F_{3/2} \rightarrow {}^4I_{11/2}$ transition peaks.

$Nd(tta)_3$ complexes were employed for the functionalization the maximum is around 350.0 nm. When the $Nd(bta)_3$ complexes were used instead the maximum is shifted slightly towards lower wavelengths – 327.0 nm for dppz-ePMO@$Nd(bta)_3$ and 336.0 nm for dppz-vSilica@$Nd(bta)_3$. Aside from the broad band, several sharp peaks (some embedded on the broad band), which could be assigned to f–f transitions of Nd^{3+} can be observed in the excitation spectra of these samples. In the case of all four materials the emission spectra consist of the three characteristic Nd^{3+} emission peaks: $^4F_{3/2} \rightarrow {}^4I_{9/2}$ (895.0–890.0 nm), $^4F_{3/2} \rightarrow {}^4I_{11/2}$ (1065.0 nm), and $^4F_{3/2} \rightarrow {}^4I_{13/2}$ (1335.0 nm). A detailed assignment of all excitation and emission peaks in these spectra can be found in Table S1.† These materials show strongest emission when they are excited into the maximum of the broad band, but as has been shown in Fig. 5 for the dppz-vSilica@$Nd(tta)_3$ materials, good luminescence properties can also be obtained when exciting in the visible region, into some of the f–f transitions of Nd^{3+} (*e.g.* at 462.0 nm or 739.0 nm).

Fig. 6 presents the combined excitation–emission spectra of the Yb^{3+} β-diketonate functionalized dppz-ePMO and dppz-vSilica compounds. A strong broad emission peak with a maximum around 985.0 nm was observed for all studied materials – dppz-ePMO@$Yb(tta)_3$, dppz-ePMO@$Yb(bta)_3$, dppz-vSilica@$Yb(tta)_3$, and dppz-vSilica@$Yb(bta)_3$ when exciting into the maximum of the broad excitation band centered around 350.0 nm (slightly varied depending on sample). In Fig. S7† the combined excitation–emission spectrum of dppz-vSilica@$YbCl_3$ has been presented for comparison.

When exciting the Er^{3+} materials at 350.0 nm one strong, broad peak located at around 1530.0–1535.0 nm, which can be assigned to the $^4I_{13/2} \rightarrow {}^4I_{15/2}$ "telecom" transition, was observed for the dppz-ePMO@$Er(tta)_3$, dppz-vSilica@$Er(bta)_3$, and dppz-vSilica@$Er(tta)_3$ materials (Fig. 7). The recorded emission spectra were very weak in all three cases. No signal was detected for the dppz-ePMO@$Er(bta)_3$ material. This is due to the strong quenching of the material, the strong quenching can also be observed for the Nd^{3+} and Yb^{3+} materials.

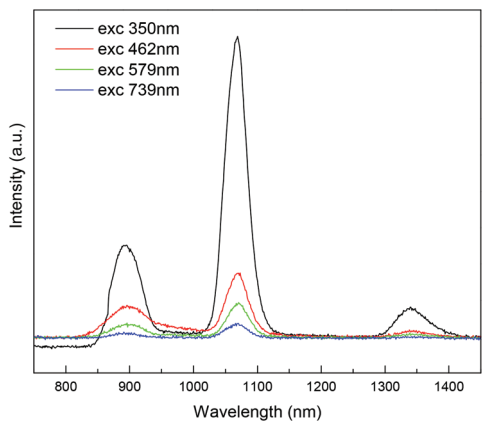

Fig. 5 Compiled emission spectra of dppz-vSilica@$Nd(tta)_3$ excited at different wavelengths.

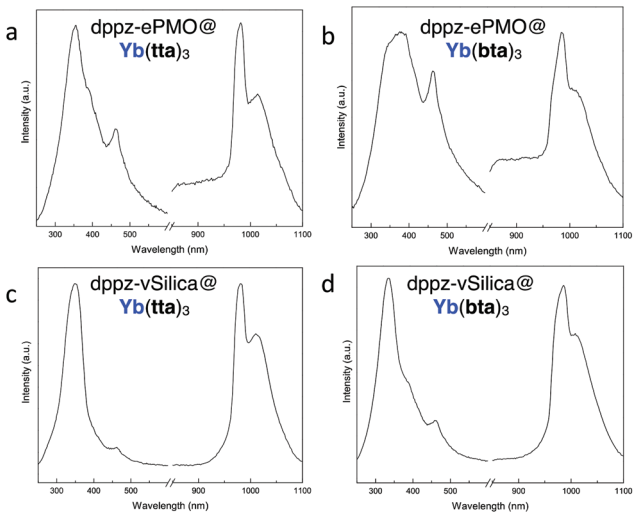

Fig. 6 Combined excitation–emission luminescence spectra of (a) dppz-ePMO@$Yb(tta)_3$, (b) dppz-ePMO@$Yb(bta)_3$, (c) dppz-vSilica@$Yb(tta)_3$, and (d) dppz-vSilica@$Yb(bta)_3$. All of the emission spectra where recorded when excited into the maximum of the broad bands and observed at the $^2F_{5/2} \rightarrow {}^2F_{7/2}$ transition peaks.

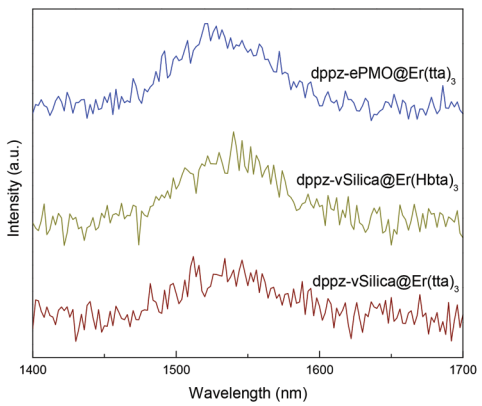

Fig. 7 Emission spectra of Er^{3+} containing materials (from top to bottom): dppz-ePMO@$Er(tta)_3$, dppz-vSilica@$Er(bta)_3$, and dppz-vSilica@$Er(tta)_3$. Only very weak emission is observed for these materials. No NIR emission was detected for the dppz-ePMO@$Er(bta)_3$ material.

In order to compare the luminescence properties of the dppz-ePMO@Ln^{3+} and dppz-vSilica@Ln^{3+} materials we have carried out decay time measurements for all of the Nd^{3+} and Yb^{3+} samples. The Er^{3+} samples were excluded from further studies due to their low luminescence intensity. For all samples the decay times were measured when exciting into the maximum of the broad ligand band and observing at the most intensive emission peak. All decay profiles have been presented in the ESI (Fig. S8–S15†) and all of the decay times have been overviewed in Table 1. The decay curves of all samples could be well fitted only when using a double-exponential function. This suggests that there is more than one coordination environment around the Ln^{3+} ions in these hybrid mesoporous materials. When comparing the decay times of

Table 1 Luminescence decay times of mesoporous materials

Sample	τ_1 (ns)/%	τ_2 (ns)/%	τ_{av} (ns)
dppz-ePMO@Nd(tta)$_3$	85/97	680/3	191
dppz-ePMO@Nd(bta)$_3$	49/99.998	614/0.002	49
dppz-vSilica@Nd(tta)$_3$	80/98	681/2	168
dppz-vSilica@Nd(bta)$_3$	47/99.999	596/0.001	47
dppz-ePMO@Yb(tta)$_3$	848/91	4776/9	2295
dppz-ePMO@Yb(bta)$_3$	753/90	4201/10	2070
dppz-vSilica@Yb(tta)$_3$	807/90	4491/10	2195
dppz-vSilica@Yb(bta)$_3$	746/90	4135/10	2039

these samples it is quite clear that the dppz-ePMO@Ln^{3+} and dppz-vSilica@Ln^{3+} materials show very similar performance. The average decay times were calculated using eqn (S1).† For example, for dppz-ePMO@Yb(tta)$_3$ the average decay time was recorded to be 2.2 μs, whereas for the equivalent dppz-vSilica@Yb(tta)$_3$ material it was 2.3 μs, which can be considered identical luminescence lifetimes within error margin.

For the dppz-ePMO@Nd(tta)$_3$ and dppz-vSilica@Nd(tta)$_3$ materials we have additionally carried out temperature dependent luminescence studies in the 10–360 K range (Fig. 8 and 9). For both materials strong emission intensity is observed at low temperature and gradually decreases with temperature increase. Yet, at some temperature point the emission intensity once again starts increasing (around 260–310 K). These changes can be attributed to the population redistributions induced by temperature.[43] A higher temperature induces a higher phonon density, increases multiphonon relaxations, and additionally the energy transfer processes from the ligands to the Ln^{3+} ions are strengthened.[44] We believe the temperature dependent luminescence trend where the emission of the sample increases at higher temperature can originate in a large part from the Ln^{3+} β-diketonate component. As we have presented in the ESI (Fig. S16†) for the Ln(tta)$_3$·2H_2O we observed a significant raise in the emission intensity with temperature increase. The temperature dependent luminescence has also been measured for the dppz-ePMO@Yb(tta)$_3$ and dppz-vSilica@Yb(tta)$_3$ samples and similar trends to those

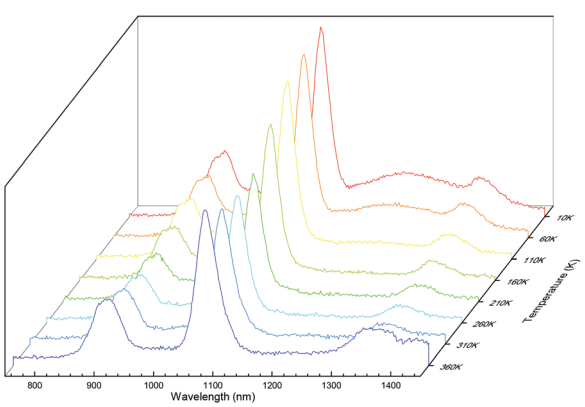

Fig. 8 Temperature dependent luminescence of the dppz-ePMO@Nd (tta)$_3$ material.

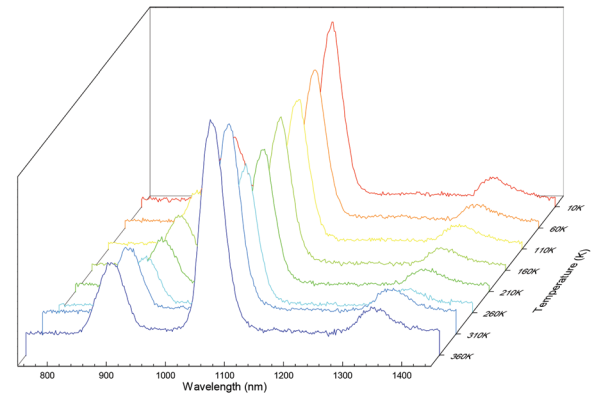

Fig. 9 Temperature dependent luminescence of the dppz-vSilica@Nd (tta)$_3$ material.

observed for the Nd^{3+} samples were also observed here (Fig. 10 and 11). In the case of the Yb^{3+} samples not only does the intensity of the sample change but also around 260 K the shape of the peak changes compared to lower temperatures.

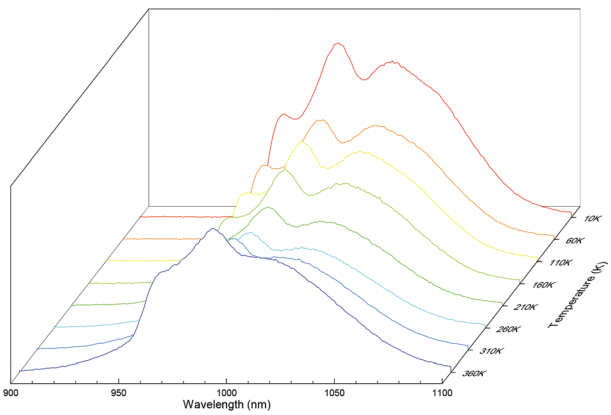

Fig. 10 Temperature dependent luminescence of the dppz-ePMO@Yb (tta)$_3$ material.

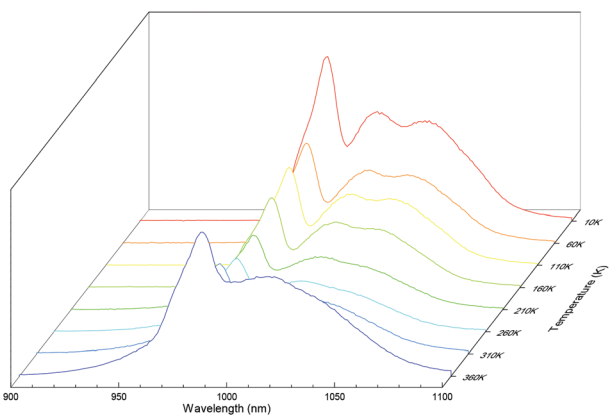

Fig. 11 Temperature dependent luminescence of the dppz-vSilica@Yb (tta)$_3$ material.

The interesting temperature dependent luminescence properties of this kind of materials could give them future applications in the field of luminescence sensors or thermometry.

As mentioned in the introduction, there are several different ways of accessing the temperature change of a material by employing luminescence features. Here, we focused on the change in the emission intensity with temperature change. Several Nd^{3+} doped materials have already been studied for their potential as luminescence thermometers, often as ratiometric thermometers.[45–47] In most cases, the intensity ratio between the $^4F_{3/2(1)} \rightarrow {}^4I_{9/2}$ and $^4F_{3/2(2)} \rightarrow {}^4I_{9/2}$ transitions (where $^4F_{3/2(1)}$ and $^4F_{3/2(2)}$ are two Stark components of the $^4F_{3/2}$ multiplet) is used to assess the ratiometric temperature parameter. It is also possible to use the $^4F_{5/2} \rightarrow {}^4I_{9/2}$ to $^4F_{3/2} \rightarrow {}^4I_{9/2}$ intensity ratio as the ratiometric temperature parameter.[45] In the case of our dppz-ePMO@NdL_3 and dppz-vSilica@NdL_3 materials this is not possible as the two Stark components of the $^4F_{3/2}$ multiplet as well as the $^4F_{5/2} \rightarrow {}^4I_{9/2}$ transition is not observed. They are usually observed only in inorganic phosphors doped with Nd^{3+} ions.[28] When analyzing the two Yb^{3+} doped materials we observed that when calculating the maximum intensity of the 986 nm/1015 nm peaks (for dppz-ePMO@Yb(tta)$_3$) or 990 nm/1025 nm peaks (for dppz-vSilica@Yb(tta)$_3$) in a certain temperature range these materials could be considered as ratiometric temperature sensors. Both materials showed a monotonic temperature behavior in the range of 110–310 K. For the dppz-ePMO@Yb(tta)$_3$ material the I_{986}/I_{1015} ratio (based on the maxima of the peaks) was calculated for measurements carried out at a temperature range of 110–310 K and has been plotted in Fig. 12a. The data points could be well fitted with eqn (1) (R^2 = 0.999). The absolute S_a and relative S_r sensitivities were calculated based on eqn (2) and (3), respectively. The data have been plotted in Fig. 12b and c. The maximum values of S_a and S_r are 0.0017 K^{-1} (at 110 K) and 0.17% K^{-1} (at 110 K), respectively.

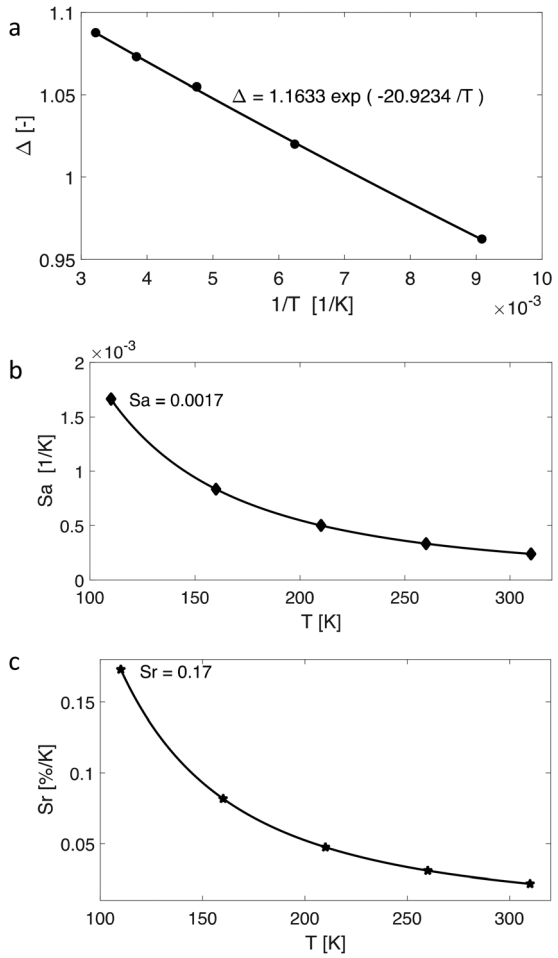

Fig. 12 (a) Plot presenting the calibration curve for dppz-ePMO@Yb(tta)$_3$ material. The points depict the experimental Δ parameter and the solid line is the best fit of the experimental points using eqn (1); (b) plot showing the absolute sensitivity S_a values at different temperatures (110–310 K) for dppz-ePMO@Yb(tta)$_3$, and (c) relative sensitivity S_r values at different temperatures (110–310 K) also for dppz-ePMO@Yb(tta)$_3$. The solid line is a guide for the eyes.

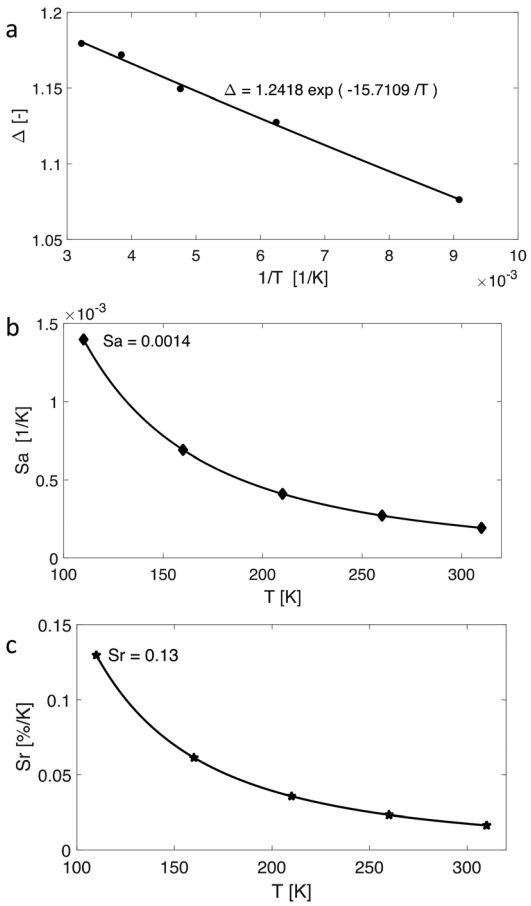

Fig. 13 (a) Plot presenting the calibration curve for dppz-vSilica@Yb(tta)$_3$ material. The points depict the experimental Δ parameter and the solid line is the best fit of the experimental points using eqn (1); (b) plot showing the absolute sensitivity S_a values at different temperatures (110–310 K) for dppz-vSilica@Yb(tta)$_3$, and (c) relative sensitivity S_r values at different temperatures (110–310 K) also for dppz-vSilica@Yb(tta)$_3$. The solid line is a guide for the eyes.

$$\Delta \approx C \exp\left(-\frac{\Delta E}{k_B T}\right) \quad (1)$$

$$S_a = \left|\frac{\partial \Delta}{\partial T}\right| \quad (2)$$

$$S_r = 100\% \times \left|\frac{1}{\Delta}\frac{\partial \Delta}{\partial T}\right| \quad (3)$$

For the dppz-vSilica@Yb(tta)$_3$ material the I_{990}/I_{1025} ratio (based on the maxima of the peaks) was calculated for measurements carried out at a temperature range of 110–310 K and has been plotted in Fig. 13a. The data points could be well fitted with eqn (1) (R^2 = 0.997). The absolute S_a and relative S_r sensitivities were calculated based on eqn (2) and (3), respectively. The data have been plotted in Fig. 13b and c. The maximum values of S_a and S_r are 0.0014 K^{-1} (at 110 K) and 0.13% K^{-1} (at 110 K), respectively. These values are slightly lower than those of the dppz-ePMO@Yb(tta)$_3$ material, but are in a similar range, thus showing comparable temperature dependent output of the two materials.

4. Conclusions

To conclude, we have reported the preparation of a mesoporous silica and a periodic mesoporous organosilica material, which were both functionalized with dipyridyl-pyridazine (dppz) units and further grafted with Nd^{3+}, Er^{3+}, and Yb^{3+} β-diketonate (2-thenoyltrifluoroacetone or benzoyltrifluoroacetone) complexes in an attempt to obtain hybrid NIR emitting materials. We have previously reported the preparation of a similarly functionalized ePMO material (functionalized with the dipyridyl-dihydropyridazine ligand) and its grafting with Eu^{3+} ions. Here, we have synthesized the dppz-ePMO and dppz-vSilica materials, which we both further functionalized with lanthanide complexes. We show that both the dppz-ePMO and dppz-vSilica are very good "platform" materials for the further functionalization with NIR emitting lanthanide ions for luminescence applications. The dppz-vSilica material was faster in preparation, and with very similar luminescence properties to the equivalent porous dppz-ePMO@Ln^{3+}. The advantage of the dppz-ePMO@Ln^3 materials is its known higher stability originating from the ePMO. Detailed luminescence studies, including temperature dependent investigations were carried out. These materials could be excited either through the broad ligand band in the UV-Vis region or through the sharp f-f transitions present in a wide range of the excitation spectra. The dppz-ePMO@Ln^{3+} and dppz-vSilica@Ln^{3+} materials did not show any significant differences in their emission intensities, decay times or temperature dependent luminescence behavior.

Temperature dependent luminescence studies of chosen Nd^{3+} and Yb^{3+} materials showed that these materials exhibit a change in emission intensity with temperature change. When the temperature increases from 10 K to 260 K the intensity gradually decreases. After 260 K the intensity starts increasing again with further temperature increases. Both the dppz-ePMO@LnL_3 and dppz-vSilica@LnL_3 materials behaved in a similar manner with temperature change. The Yb^{3+} materials were evaluated for their potential use as ratiometric temperature sensors. They showed monotonic behavior in the temperature range 110–310 K.

Acknowledgements

A. M. K. acknowledges Ghent University's Special Research Fund (BOF) for a Postdoctoral Mandate (project BOF15/PDO/091). D. E. and F. J. R.-S. acknowledge funding of this research by the Spanish Ministry of Economy and Competitiveness (Project MAT2013-44463-R), Andalusian Regional Government (FQM-346 group), Andalucía Talent Hub and Feder Funds.

References

1 G. Liu and X. Chen, *Handbook on the Physics and Chemistry of Rare Earths*, ed. K. A. Gschneidner Jr., J.-C. G. Bünzli and V. K. Pecharsky, Elsevier Science, Amsterdam, 2007, ch. 233, vol. 37, pp. 99–169.
2 J. C. G. Bunzli and C. Piguet, *Chem. Soc. Rev.*, 2005, **34**, 1048–1077.
3 S. V. Eliseeva and J.-C. G. Bünzli, *Chem. Soc. Rev.*, 2010, **39**, 189–227.
4 K. Binnemans, *Chem. Rev.*, 2009, **109**, 4283–4374.
5 D. Esquivel, A. M. Kaczmarek, C. Jimenez-Sanchidrian, R. Van Deun, F. J. Romero-Salguero and P. Van Der Voort, *J. Mater. Chem. C*, 2015, **3**, 2909–2917.
6 X. Guo, H. Guo, L. Fu, H. Zhang, R. Deng, L. Sun, J. Feng and S. Dang, *Microporous Mesoporous Mater.*, 2009, **119**, 252–258.
7 L. Sun, W. Mai, S. Dang, Y. Qiu, W. Deng, L. Shi, W. Yan and H. Zhang, *J. Mater. Chem.*, 2012, **22**, 5121–5127.
8 L. N. Sun, H. J. Zhang, C. Y. Peng, J. B. Yu, Q. G. Meng, L. S. Fu, F. Y. Liu and X. M. Guo, *J. Phys. Chem. B*, 2006, **110**, 7249–7258.
9 L. N. Sun, H. J. Zhang, J. B. Yu, S. Y. Yu, C. Y. Peng, S. Dang, X. M. Guo and J. Feng, *Langmuir*, 2008, **24**, 5500–5507.
10 C. M. Granadeiro, S. O. Ribeiro, A. M. Kaczmarek, L. Cunha-Silva, P. L. Almeida, S. Gago, R. Van Deun, B. de Castro and S. S. Balula, *Microporous Mesoporous Mater.*, 2016, **234**, 248–256.
11 B. Yan and B. Zhou, *J. Photochem. Photobiol., A*, 2008, **195**, 314–322.
12 Y. Li, B. Yan and H. Yang, *J. Phys. Chem. C*, 2008, **112**, 3959–3968.
13 D. B. Ambili Rai, S. Biju and M. L. P. Reddy, *J. Mater. Chem.*, 2009, **19**, 7976–7983.
14 S. M. Bruno, A. C. Coelho, R. A. S. Ferreira, L. D. Carlos, M. Pillinger, A. A. Valente, P. Ribeiro-Claro and I. S. Goncalves, *Eur. J. Inorg. Chem.*, 2008, 3786–3795.

15 V. Divya, S. Biju, R. Luxmi Varma and M. L. P. Reddy, *J. Mater. Chem.*, 2010, **20**, 5220–5227.
16 H. R. Li, J. Lin, L. S. Fu, J. F. Guo, Q. G. Meng, F. Y. Liu and H. J. Zhang, *Microporous Mesoporous Mater.*, 2002, **55**, 103–107.
17 Y.-J. Li, B. Yan and L. Wang, *Dalton Trans.*, 2011, **40**, 6722–6731.
18 H. Takeda, M. Ohashi, T. Tani, O. Ishitani and S. Inagaki, *Inorg. Chem.*, 2010, **49**, 4554–4559.
19 H. Takeda, Y. Goto, Y. Maegawa, T. Ohsuna, T. Tani, K. Matsumoto, T. Shimada and S. Inagaki, *Chem. Commun.*, 2009, 6032–6034.
20 Y. Li, B. Yan and Y. J. Li, *Microporous Mesoporous Mater.*, 2010, **132**, 87–93.
21 S. Biju, Y. K. Eom, J. C. G. Bunzli and H. K. Kim, *J. Mater. Chem. C*, 2013, **1**, 3454–3466.
22 N. M. Shavaleev, S. J. A. Pope, Z. R. Bell, S. Faulkner and M. D. Ward, *Dalton Trans.*, 2003, 808–814.
23 D. Jaque and F. Vetrone, *Nanoscale*, 2012, **4**, 4301–4326.
24 A. Benayas, B. del Rosal, A. Perez-Delgado, K. Santacruz-Gomez, D. Jaque, G. A. Hirata and F. Vetrone, *Adv. Optical Mat.*, 2015, **3**, 1–8.
25 L. Li, Y. Zhu, X. Zhou, C. D. S. Brites, D. Ananias, Z. Lin, F. A. A. Paz, J. Rocha, W. Hunag and L. D. Carlos, *Adv. Funct. Mater.*, 2016, **26**, 8677–8684.
26 Y. Ciu, F. Zhu, B. Chen and G. Qian, *Chem. Commun.*, 2015, **51**, 7420–7431.
27 J. Rocha, C. D. S. Brites and L. D. Carlos, *Chem. – Eur. J.*, 2016, **22**, 1–15.
28 A. Benayas, B. del Rosal, A. Perez-Delgado, K. Santacruz-Gomez, D. Jaque, G. A. Hirato and F. Vetrone, *Adv. Funct. Mater.*, 2015, **3**, 687–694.
29 J. Liu, R. Van Deun and A. M. Kaczmarek, *J. Mater. Chem. C*, 2016, **4**, 9937–9941.
30 S. Balabhadra, M. L. Dabasu, C. D. S. Brites, L. A. O. Nunes, O. L. Malta, J. Rocha, M. Bettinelli and L. D. Carlos, *Nanoscale*, 2015, **7**, 17261–17267.
31 M. S. Robillard, H. M. Janssen, W. ten Hoeve and R. M. Versreegen, *US pat*, 9421274B2, 2016.
32 C. Vercaemst, M. Ide, B. Allaert, N. Ledoux, F. Verpoort and P. Van Der Voort, *Chem. Commun.*, 2007, 2261–2263.
33 G. P. Sagitullina, L. V. Glyzdinskaya and R. S. Sagitullin, *Khim. Geterotsikl. Soedin.*, 2005, 858–863.
34 L. R. Melby, E. Abramson, J. C. Caris and N. J. Rose, *J. Am. Chem. Soc.*, 1964, **86**, 5117–5125.
35 K. Binnemans, P. Lenaerts, K. Driesen and C. Gorller-Walrand, *J. Mater. Chem.*, 2004, **14**, 191–195.
36 D. Esquivel, E. De Canck, C. Jimenez-Sanchidrian, P. Van Der Voort and J. Romero-Salguero, *J. Mater. Chem.*, 2011, **21**, 10990–10998.
37 C. Vercaemst, J. T. A. Jones, Y. Z. Khimyak, J. C. Martins, F. Verpoort and P. Van Der Voort, *Phys. Chem. Chem. Phys.*, 2008, **10**, 5349–5352.
38 L. Sun, Y. Qiu, T. Liu, J. Z. Zhang, S. Dang, J. Feng, Z. Wang, H. Zhang and L. Shi, *ACS Appl. Mater. Interfaces*, 2013, **5**, 9585–9593.
39 Y. Liu, L. Sun, J. Liu, Y.-X. Peng, X. Ge, L. Shi and W. Huang, *Dalton Trans.*, 2015, **44**, 237–246.
40 Y.-J. Gu and B. Yan, *J. Colloid Interface Sci.*, 2013, **393**, 36–43.
41 P. Yang, Z. Quan, C. Li, H. Lian, S. Huang and J. Lin, *Microporous Mesoporous Mater.*, 2008, **116**, 524–531.
42 X. Lian and B. Yan, *New J. Chem.*, 2013, **37**, 1–3.
43 L. Labrador-Paez, C. Perez-Rodriguez, S. Rios, D. Alonso, J. M. Caceres and I. R. Martin, *Sens. Actuators, A*, 2015, **233**, 422–426.
44 X. Xu, Z. Wang, P. Lei, Y. Yu, S. Yao, S. Song, X. Liu, Y. Su, L. Dong, J. Feng and H. Zhang, *ACS Appl. Mater. Interfaces*, 2015, **7**, 20813–20819.
45 U. Rocha, C. Jacinto, W. F. Silva, I. Guedes, A. Benayas, L. M. Maestro, M. A. Elias, E. Bovero, F. van Veggel, J. A. G. Sole and D. Jaque, *ACS Nano*, 2013, **7**, 1188–1199.
46 O. A. Savchuk, J. J. Carvajal, L. De la Cruz, P. Haro Gonzalez, M. Aguilo and F. Diaz, *J. Mater. Chem. C*, 2016, **4**, 7397–7405.
47 D. Wawrzynczyk, A. Bednarkiewicz, M. Nyk, W. Strek and M. Samoc, *Nanoscale*, 2012, **4**, 6959–6961.